JACS
JOURNAL OF THE AMERICAN CHEMICAL SOCIETY
Communication
pubs.acs.org/JACS

High Stability, High Activity Pt/ITO Oxygen Reduction Electrocatalysts

Ying Liu and William E. Mustain*

Department of Chemical and Biomolecular Engineering, University of Connecticut, 191 Auditorium Drive, Storrs, Connecticut 06269, United States

Supporting Information

ABSTRACT: Sn-doped indium oxide (ITO) nanoparticles (NPs) were conceived as a high stability noncarbon support for Pt NPs, and the activity and stability of Pt/ITO for the oxygen reduction reaction (ORR) were probed. Sn was employed as the In_2O_3 dopant to exploit the strong interaction between Sn and Pt that was previously reported to enhance the activity of Pt on Pt/SnO_2, while concomitantly avoiding the intrinsic stability limitations of SnO_2 and leveraging the high stability of bulk In_2O_3 at ORR relevant potentials. The mass activity of Pt was extremely high on Pt/ITO, 621 ± 31 mA/mg_{Pt}, which far exceeded the 2015 DOE goal for Pt mass activity of 440 mA/mg_{Pt}. The enhanced ORR activity was linked to the faceting of the Pt NPs, which overwhelmingly consisted of Pt (111) facets. The stability of Pt/ITO was also very impressive, with the electrochemically active area unchanged and the Pt half wave potential shifting only 4 mV over 1000 potential cycles to 1.4 V vs RHE, a very harsh condition for ORR electrocatalysts where state-of-the-art Pt/C electrocatalysts typically show very poor stability.

Proton exchange membrane fuel cells (PEMFCs) have drawn significant attention as a 21st century alternative to environmentally unfriendly power sources, for example, fossil fuel power plants and internal combustion engines. However, to make PEMFCs economically viable, one of the main problems to be solved is finding catalysts with sufficient activity and stability for the oxygen reduction reaction (ORR).[1,2] To address this problem, a number of methods have been proposed for developing an electrocatalyst with improved performance, including alloying Pt with secondary transition metals or depositing monolayers of Pt onto other fine metal particles to create core−shell structures.[3−9] Although Pt supported on carbon is still the most widely used catalyst, oxide supports as alternatives to carbon have shown improved corrosion resistance and reduced electrochemically active area (ECA) degradation rates.[10−17] In addition, oxide supports are also able to affect the electrocatalytic activity of the supported noble metals due to metal−support interactions. These interactions manifest in several ways including (i) modification of the electronic states or Fermi level of Pt that pushes the formation of Pt−OH groups to higher potentials;[18] (ii) spillover of OH groups onto the oxide support; and (iii) reduction of OH coverage by lateral repulsion between Pt−OH and oxide surfaces.[19]

Ota et al. found that tin dioxide (SnO_2) influences the oxidation and reduction behavior of supported Pt, where the formation of Pt-oxide species at high potentials was suppressed.[20] Oxide suppression has the potential to improve both the ORR activity of Pt by providing a clean surface over a wide potential range and the stability of Pt since oxide species are a key intermediate in the Pt dissolution process.[21,22] However, raw SnO_2 suffers from two important limitations that may preclude its use as a PEMFC cathode support. First, SnO_2 undergoes redox processes at potentials relevant to the ORR and is at least somewhat unstable. Second, SnO_2 is a wide band gap semiconductor with electrical resistivity varying from 10 to 10^6 Ω·cm;[23,24] this high electrical resistance within the catalyst layer would be detrimental to fuel cell performance. One way to overcome these limitations to realize a high stability support is to dope Sn into a high conductivity material with good stability in acid at ORR relevant potentials, such as In_2O_3.[25] In this study, tin was doped into the structure of indium oxide, and the resulting tin-doped indium oxide (ITO) particles with high conductivity were used as supports for Pt. The ORR activity and stability of Pt/ITO were explored to understand the enhancement of the ORR on Pt due to the interaction between Pt and surface Sn.

To prepare the ITO nanoparticles (NPs), a slurry of precursors, indium acetylacetonate ($In(acac)_3$) and tin bis(acetylacetonate) dichloride ($Sn(acac)_2Cl_2$) with variable ratios (Table S1) was prepared in oleylamine and heated at 250 °C for 3 h in air to produce a dark yellow suspension. The ITO NPs precipitated by the addition of ethanol to the suspension, and the supernatant was removed by centrifugation. Washing with ethanol was repeated and gave a white powder of ITO NPs. The ITO powder was heated at 80 °C under vacuum for 24 h and was then heated at 500 °C for 3 h in air.

Figure 1a shows XRD patterns for tin-doped indium oxide NPs with varying Sn doping. All patterns showed a bixbyite In_2O_3 cubic structure (JCPDS 06-0416) with no secondary phases, indicating the effective incorporation of Sn into the In_2O_3. The lattice parameters, calculated from the XRD patterns, are plotted as a function of the Sn concentration in Figure 1b. At 1 atom % Sn, the lattice parameter decreased slightly compared to that of the undoped In_2O_3 due to the replacement of In^{3+} (0.8 Å) by Sn^{4+} (0.71 Å), which is smaller. At 5 atom % Sn, the lattice parameter reached an inflection point where the lattice parameter increased with the concentration of Sn. One possible explanation for the lattice expansion is incorporation of larger

Received: August 2, 2012
Published: December 27, 2012

   dx.doi.org/10.1021/ja307635r | J. Am. Chem. Soc. 2013, 135, 530−533

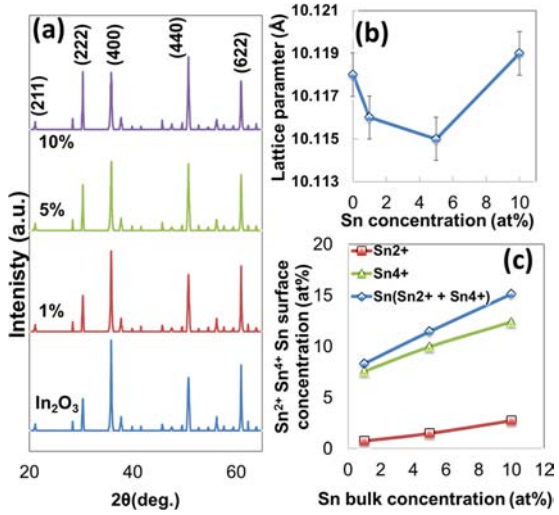

Figure 1. (a) Powder XRD patterns for pure tin-doped indium oxide crystals with various Sn content. (b) Lattice parameter of tin-doped indium oxide as a function of Sn content. (c) Variation of the concentration of Sn^{2+} and Sn^{4+} ions as a function of Sn concentration.

Sn^{2+} ions (1.12 Å) at In^{3+} sites, which was confirmed by XPS (Figure 1c). A detailed analysis of the XPS data is provided in the Supporting Information (SI).

Figure S1 shows the XPS spectra of Sn $3d_{5/2}$ in tin-doped indium oxide NPs with various Sn concentrations. The Sn $3d_{5/2}$ peaks shifted toward lower binding energy as the Sn concentration increased. Deconvoluted peaks for Sn^{4+} (487.1 eV) and Sn^{2+} (486.1 eV) were obtained to determine the relative concentrations of Sn^{2+} and Sn^{4+} species. By combining these relative concentrations and the total Sn concentrations in these ITO NPs, the Sn^{2+} and Sn^{4+} content were obtained and are shown in Figure 1c. At 1 atom % Sn, almost all of the Sn was in the Sn^{4+} state. As the Sn concentration increased, the content of the Sn^{2+} ion increased from 0.75% to 2.73%, whereas that of Sn^{4+} increased from 7.57% to 12.4%. It is worth noting that the Sn^{2+} ion content increased greatly relative to that of the Sn^{4+} ion as the Sn concentration increased. Since the In^{3+} is larger than Sn^{4+} and smaller than Sn^{2+}, the structural disturbances due to the differences in ionic radii and electrical charges between Sn and In ions can be relaxed through substitution by Sn^{2+}. Thus, the change of the lattice parameters of the tin-doped indium oxides when the Sn content increases can be explained by substitutional incorporation of both Sn^{4+} and Sn^{2+}. Another important consideration is that the surface concentration of Sn is more than twice that of the bulk because of Sn surface segraration in the ITO stucture.

The structure of the ITO NPs was examined by high-resolution transmission electron microscopy. The 5 atom % tin-doped indium oxide NPs prepared without high temperature treatment had an average size of 5 nm (Figure 2a). The amorphous edges indicate that these NPs were not well-crystallized, especially compared with those heated at 500 °C for 3 h (Figure 2b), which were fully crystallized with an average size of 18 nm. TEM images of individual NPs (Figure 2c–e) show their crystalline structure with a highly ordered continuous fringe pattern over a range of Sn concentrations. Most of the exposed facets were found to be {222}, although some {220} and {022} were also identified. We also found that the heat treatment temperature impacted the ITO morphology, which is discussed in the SI.

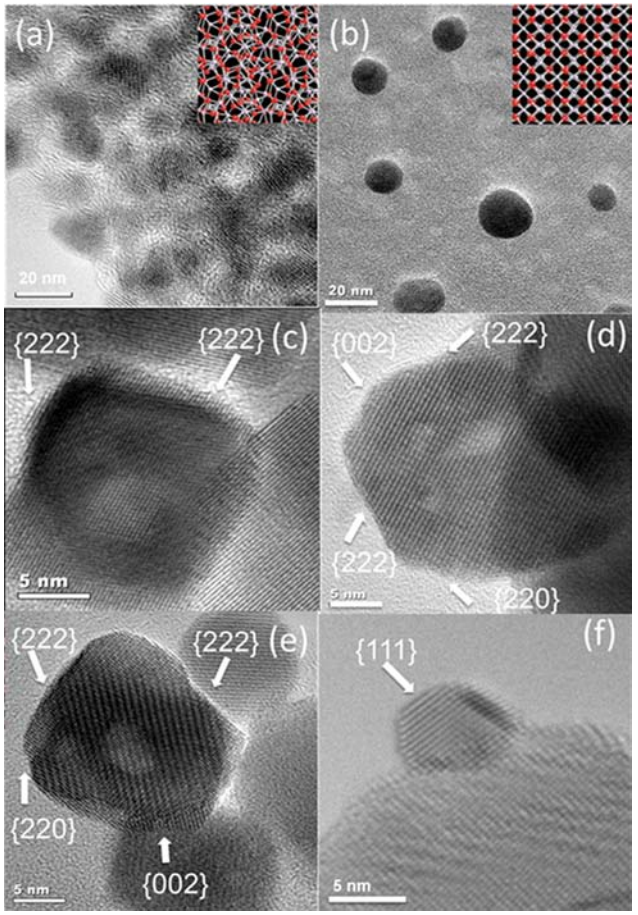

Figure 2. TEM images of tin-doped indium oxide NPs: (a) unheated 5 atom %, inset shows an uncrystallized structure; (b) Heated at 500 °C, 5 atom % (inset shows a fully crystallized structure. HRTEM images of those (c) heated at 500 °C, 1 atom %; (d) heated at 500 °C, 5 atom %; and (e) heated at 500 °C, 10 atom %. (f) HRTEM image of Pt NP supported on ITO prepared by heating to 500 °C, 5 atom %.

Pt clusters were deposited on the ITO NPs through galvanic displacement of Cu by Pt. TEM images of the product Pt/ITO reveal that the Pt NPs were well dispersed on the ITO surface (Figure S2), which was also confirmed by XPS (Figure S3). Energy-dispersive X-ray spectroscopy applied directly to these particles showed the presence of ca. 20 wt % Pt on ITO NPs. The Pt loading was also confirmed by the copper deposition/stripping charge, detailed in the SI. Pt/ITO was further characterized by HRTEM; Figure 2f shows the tight attachment of a characteristic Pt NP to the ITO surface with a diameter of ~4 nm. In addition, the surface of the Pt NP was dominated by {111} facets and revealed continuous lattice fringes from the ITO substrate to supported Pt particles, indicating that the Pt was grown epitaxially on the ITO surface.

Figure S5 shows cyclic voltammograms (CVs) for Pt/ITO and Pt/C catalysts (20 wt % Pt on Vulcan XC-72) recorded at room temperature in a N_2-purged 0.1 M $HClO_4$ solution at a sweep rate of 50 mV/s. All potentials are discussed relative to the reversible hydrogen electrode (RHE). The CVs exhibited two distinct potential regions associated with H_{upd} adsorption/desorption processes ($H^+ + e^- = H_{upd}$) between $0 < E < 0.35$ V and the formation of a OH_{ad} layer ($2H_2O = OH_{ad} + H_3O^+ + e^-$) beyond 0.6 V, where H_{upd} and OH_{ad} refer to underpotentially deposited hydrogen and adsorbed hydroxyl species, respectively.

dx.doi.org/10.1021/ja307635r | J. Am. Chem. Soc. 2013, 135, 530–533

The electrochemically active surface area (ECSA) was calculated by integrating the double layer corrected H_{upd} charge in the cathodic scan and dividing by a value of 210 $\mu C/cm^2$ for the adsorption of a hydrogen monolayer on polycrystalline Pt. The specific ECSA of Pt/ITO (83.1 m^2/g_{Pt}) was found to be three times that of Pt/C (27.3 m^2/g_{Pt}).

ORR measurements were performed in O_2-saturated 0.1 M $HClO_4$ electrolyte using a thin film catalyst deposited onto a glassy carbon disk electrode at rt. Each experiment was performed at least five times to ensure reproducibility. The Pt/ITO loading was 9.40 $\mu g/cm^2$, whereas the loading was 27.6 $\mu g/cm^2$ for the Pt/C. Rotating-disk electrode (RDE) experiments were performed to reveal the ORR kinetics of Pt/ITO (Figure 3a) and Pt/C. The linearity of the Koutecky–Levich plots and

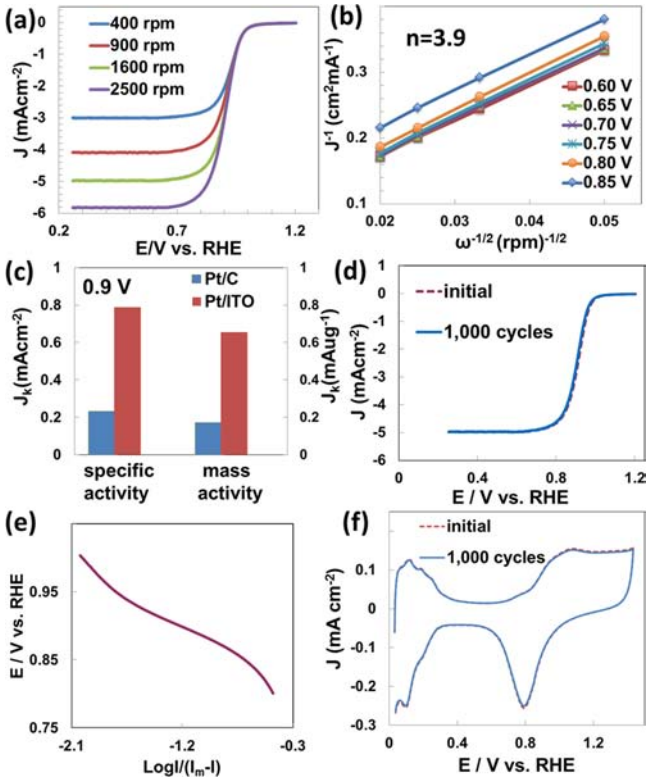

Figure 3. (a) Room temperature rotating disk voltammograms of Pt/ITO electrocatalyst in O_2-saturated 0.1 M $HClO_4$. Sweep rate, 5 mV/s. (b) Corresponding Koutecky–Levich plots (J^{-1} vs $\omega^{-0.5}$) at different potentials. (c) Mass activity and specific activity at 0.9 V vs RHE for Pt/ITO and Pt/C. Mass and specific activities are given as kinetic current densities (j_k) normalized in reference to the loading amount and ECSA of metal, respectively. (d) Polarization curves for the O_2 reduction reaction on Pt/ITO catalysts on a rotating disk electrode, before and after 1000 cycles. Sweep rate, 10 mV/s; rotating rate, 1600 rpm. (e) The Tafel plot derived by the mass-transport correction of the first RDE data. (f) Voltammetry curves for Pt/ITO before and after 1000 cycles. Sweep rate, 10 mV/s (SI).

near parallelism of the fitting lines suggest first-order reaction kinetics and similar electron transfer numbers for ORR at different potentials (Figure 3b). The electron transfer number was calculated to be ~3.9 at 0.6–0.85 V from the slopes of Koutecky–Levich plots, suggesting Pt/ITO favors a $4e^-$ oxygen reduction process. Polarization curves for the ORR on the catalysts are shown in Figure 3d. The diffusion-limiting currents were obtained in the potential region below 0.6 V, whereas a mixed kinetic-diffusion control region existed between 0.7 and 1.1 V. The kinetic current was calculated from the ORR polarization curve by using mass-transport correction to compare the specific activity of the catalysts. The Pt/ITO catalyst exhibited a specific activity of 0.750 ± 0.04 mA/cm^2 at 0.9 V, which was 3 times greater than that of Pt/C (0.235 0.01 ± mA/cm^2). After normalization to the loading amount of Pt metal, the mass activity of Pt/ITO catalyst was found to be 621 ± 31 mA/mg_{Pt}, which was 4 times greater than that of Pt/C (156 ± 9 mA/mg_{Pt}). A characteristic voltammogram for Pt/ITO is presented in Figure 3c. The value for Pt/C was nearly identical to the literature accepted value reported by Gasteiger et al.,[26] validating our experimental setup and approach.

The higher specific activity of the Pt/ITO is likely a result of the synergistic effects between the surface Sn of ITO and the supported Pt NPs. Considering the small changes in the ITO lattice parameter as a function of Sn content, it is unlikely that lattice strain was the root cause for electron transfer between the catalyst and support, which suggests that electronic effects play a larger role in determining where the Pt NPs are deposited and their shape. Another important effect is the preferential exposure of {111} facets on the Pt NPs on Pt/ITO compared to Pt NPs supported on carbon blacks, which typically contain a mix of {100} and {111} facets.[27] The ORR activity on low-index crystallographic facets of Pt in a nonadsorbing electrolyte such as perchloric acid is known to increase on the order of Pt(100) ≪ Pt(111) < Pt(110), with a minor difference in catalytic activity between Pt(111) and Pt(110). This difference in ORR activity most likely arises from the structure-sensitive inhibiting effect of OH_{ad} species on Pt(*hkl*), which blocks the active site for O_2 adsorption and thus retards the ORR kinetics.

The stability of the Pt/ITO catalysts was determined by CV between 0.0 and 1.4 V. 1.4 V was selected as the upper threshold potential to ensure surface oxidation/reduction cycles on Pt, which involves the formation of PtOH and PtO derived from the oxidation of water, which causes the dissolution of Pt. High potential treatment also mimics PEMFC startup/shutdown conditions where Pt/C catalysts suffer from very poor stability.[6] The stability test was conducted by applying potential sweeps at the rate of 10 mV/s to a thin-film rotating disk electrode in an O_2-saturated 0.1 M $HClO_4$ solution at rt. After 1000 cycles, changes in the Pt ECSA and electrocatalytic activity of the ORR were determined. The stability of the Pt/ITO catalyst was far superior to that of Pt/C. The catalytic activity of Pt/ITO, measured by the linear potential sweeps, showed only a 4 mV degradation in half-wave potential over the cycling period (Figure 3c). In contrast, the shift in the half-wave potential for Pt/C was 20 mV (Figure S6). Voltammetry was again used to determine the Pt surface area of Pt/ITO and Pt/C by measuring the H adsorption before and after potential cycling. Integrating the charge between 0 and 0.35 V associated with H adsorption for Pt/ITO showed no recordable loss of Pt ECSA (Figure 3d). However, for Pt/C, only ~65% of the original ECSA remained after potential cycling (Figure S6).

The structure of the Pt/ITO catalysts after stability testing was examined by TEM (Figure 4a). Several small holes appeared on the ITO surface due to the corrosion and dissolution of the surface Sn. This was also confirmed by XPS (Figure 4b–d), which shows that surface In existed only as In_2O_3 even after 1000 cycles; however, for the surface Sn, the percentage of Sn^{4+} converted from 91% for the freshly prepared Pt/ITO to 28% after 1000 cycles (Table S2). This is an interesting result since the Pt/ITO showed very little performance loss during cycling. This suggests that the strong interaction between Pt and ITO

dx.doi.org/10.1021/ja307635r | J. Am. Chem. Soc. 2013, 135, 530–533

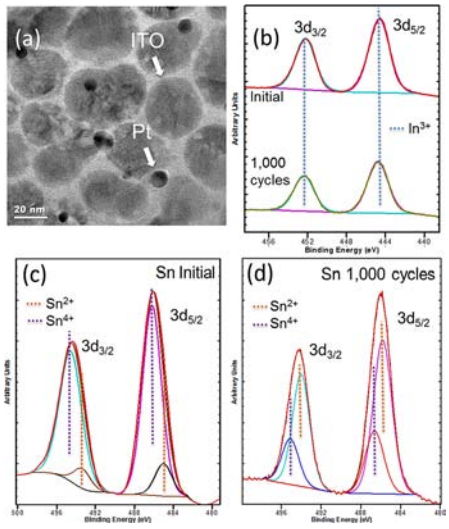

Figure 4. (a) TEM image of Pt/ITO electrocatalyst after 1000 cycles. XPS spectra of (b) In 3d and Sn 3d of Pt/ITO (c) before and (d) after 1000 cycles.

limits the surface Sn dissolution to those parts of ITO without supported Pt, which maintains the activity of Pt/ITO during the ORR.

It was found that the catalytic activity of Pt supported on ITO electrocatalysts for ORR can be enhanced drastically through synergistic effects between surface Sn and Pt, including preferential Pt faceting, which maximized the surface area of the Pt {111} facet that is highly active toward ORR. Although some other catalysts have shown mass activity at 0.9 V vs RHE > 1300 mA/mg_{Pt} (i.e., PtIrNi[28]), and specific activity ≈ 1.4 mA/cm^2 (i.e., Pt_3Co[29]), the stabilities of these catalysts have not been reported. Also, in both of the above cases, these catalysts have a very high platinum group metal content and are significantly more expensive than commercial Pt/C. For Pt/ITO, In and Sn, though more expensive than C, are relatively low cost materials, especially when compared to Co and Ir. In addition, high stability has already been achieved in this design, while the minor degradation is assumed to be due to the surface dissolution of Sn species. Since ITO, particularly the surface Sn oxide, is not thermodynamically stable in acid under normal fuel cell operating temperatures, the dissolved cations could cause further problems in fuel cell applications. Therefore, future work will focus on improving the long-term stability of Pt/ITO, and fuel cell performance using a Pt/ITO catalyst layer as the cathode will also be studied. In summary, Pt/ITO is a very promising candidate as a next generation catalyst for PEMFCs. Also, the method for introducing desired elements as dopants in a desired lattice structure, which possesses certain preferred facets, may also be useful for the development of catalysts beyond fuel cell applications.

■ ASSOCIATED CONTENT

Supporting Information

Experimental details. This material is available free of charge via the Internet at http://pubs.acs.org.

■ AUTHOR INFORMATION

Corresponding Author

mustain@engr.uconn.edu.

Notes

The authors declare no competing financial interest.

■ ACKNOWLEDGMENTS

This work was funded by the U.S. Department of Energy Office of Basic Energy Sciences, Grant No. DE-FG02 10ER16200. The authors also acknowledge the Institute of Materials Science and the Center for Clean Energy Engineering at the University of Connecticut for free use of the physical characterization equipment.

■ REFERENCES

(1) Debe, M. K. *Nature* **2012**, *486*, 43.
(2) Gasteiger, H. A.; Marković, N. M. *Science* **2009**, *324*, 48.
(3) Mukerjee, S.; Srinivasan, S. *J. Electroanal. Chem.* **1993**, *357*, 201.
(4) Mukerjee, S.; Srinivasan, S.; Soriaga, M. P.; McBreen, J. *J. Electrochem. Soc.* **1995**, *142*, 1409.
(5) Adzic, R.; Zhang, J.; Sasaki, K.; Vukmirovic, M.; Shao, M.; Wang, J.; Nilekar, A.; Mavrikakis, M.; Valerio, J.; Uribe, F. *Top. Catal.* **2007**, *46*, 249.
(6) Shrestha, S.; Liu, Y.; Mustain, W. E. *Catal. Rev.* **2011**, *53*, 256.
(7) Huang, S.-Y.; Ganesan, P.; Park, S.; Popov, B. N. *J. Am. Chem. Soc.* **2009**, *131*, 13898.
(8) Liang, Y.; Li, Y.; Wang, H.; Zhou, J.; Wang, J.; Regier, T.; Dai, H. *Nat. Mater.* **2011**, *10*, 780.
(9) Wu, G.; More, K. L.; Johnston, C. M.; Zelenay, P. *Science* **2011**, *332*, 443.
(10) Lei, B.; Xue, J.; Jin, D.; Ni, S.; Sun, H. *Rare Metals* **2008**, *27*, 445.
(11) Shim, J.; Lee, C.-R.; Lee, H.-K.; Lee, J.-S.; Cairns, E. J. *J. Power Sources* **2001**, *102*, 172.
(12) Wang, M.; Guo, D.-j.; Li, H.-l. *J. Solid State Chem.* **2005**, *178*, 1996.
(13) Ioroi, T.; Siroma, Z.; Fujiwara, N.; Yamazaki, S.-i.; Yasuda, K. *Electrochem. Commun.* **2005**, *7*, 183.
(14) Cui, X.; Shi, J.; Chen, H.; Zhang, L.; Guo, L.; Gao, J.; Li, J. *J. Phys. Chem. B* **2008**, *112*, 12024.
(15) Lee, K.-S.; Park, I.-S.; Cho, Y.-H.; Jung, D.-S.; Jung, N.; Park, H.-Y.; Sung, Y.-E. *J. Catal.* **2008**, *258*, 143.
(16) Vayssilov, G. N.; Lykhach, Y.; Migani, A.; Staudt, T.; Petrova, G. P.; Tsud, N.; Skála, T.; Bruix, A.; Illas, F.; Prince, K. C.; Matolín, V. r.; Neyman, K. M.; Libuda, J. *Nat. Mater.* **2011**, *10*, 310.
(17) Ho, V. T. T.; Pan, C.-J.; Rick, J.; Su, W.-N.; Hwang, B.-J. *J. Am. Chem. Soc.* **2011**, *133*, 11716.
(18) Baturina, O. A.; Garsany, Y.; Zega, T. J.; Stroud, R. M.; Schull, T.; Swider-Lyons, K. E. *J. Electrochem. Soc.* **2008**, *155*, B1314.
(19) Sasaki, K.; Zhang, L.; Adzic, R. R. *Phys. Chem. Chem. Phys.* **2008**, *10*, 159.
(20) Nakada, M.; Ishihara, A.; Mitsushima, S.; Kamiya, N.; Ota, K.-i. *Electrochem. Solid-State Lett.* **2007**, *10*, F1.
(21) Darling, R. M.; Meyers, J. P. *J. Electrochem. Soc.* **2003**, *150*, A1523.
(22) Darling, R. M.; Meyers, J. P. *J. Electrochem. Soc.* **2005**, *152*, A242.
(23) Kohnke, E. E. *J. Phys. Chem. Solids* **1962**, *23*, 1557.
(24) Saadeddin, I.; Pecquenard, B.; Manaud, J. P.; Decourt, R.; Labrugère, C.; Buffeteau, T.; Campet, G. *Appl. Surf. Sci.* **2007**, *253*, 5240.
(25) Koller, K. B.; Hawkridge, F. M. *J. Electroanal. Chem. Interfac.* **1988**, *239*, 291.
(26) Gasteiger, H. A.; Kocha, S. S.; Sompalli, B.; Wagner, F. T. *Appl. Catal., B* **2005**, *56*, 9.
(27) Tian, N.; Zhou, Z.-Y.; Sun, S.-G.; Ding, Y.; Wang, Z. L. *Science* **2007**, *316*, 732.
(28) Kuttiyiel, K. A.; Sasaki, K.; Choi, Y.; Su, D.; Liu, P.; Adzic, R. R. *Energy Environ. Sci.* **2012**, *5*, 5297.
(29) Chen, S.; Sheng, W.; Yabuuchi, N.; Ferreira, P. J.; Allard, L. F.; Shao-Horn, Y. *J. Phys. Chem. C* **2008**, *113*, 1109.